POLITECNICO DI TORINO
Repository ISTITUZIONALE

Modelling of magnetic bead transport in a microvascular network

(Article begins on next page)

19 April 2024

Modelling of magnetic bead transport in a microvascular network

Marta Vicentini[a,b], Riccardo Ferrero[a], Alessandra Manzin[a]

[a]Istituto Nazionale di Ricerca Metrologica (INRIM), Strada delle Cacce 91, 10135 Torino, Italy
[b]Politecnico di Torino, Corso Duca degli Abruzzi 24, 10129 Torino, Italy

Corresponding author:

Marta Vicentini

Istituto Nazionale di Ricerca Metrologica

Strada delle Cacce 91

10135 Torino, Italy

tel. +39-011-3919830

e-mail: m.vicentini@inrim.it

Abstract

In *in vivo* applications of magnetic particles one crucial aspect is the control of their transport in the tissue microvasculature and their release to target areas. These mechanisms can be driven and influenced by external magnetic fields with large gradients. Experimental results can be elucidated with the aid of *in silico* models that can also be employed to design optimized multifunctional particles and magnetic sources. In this framework, we have developed a numerical model that enables us to calculate the trajectory of an ensemble of magnetic nano/microbeads injected in a blood vessel and manipulated by an applied magnetic field. The model combines Navier-Stokes equations for the fluid dynamics simulation of blood flow with classical Newtonian mechanics for bead motion, performing the analysis in a 3D vessel segment reconstructed from a computed tomography scan. The numerical model is applied to study the influence of bead properties (size and magnetic moment) on both transport and adhesion rate, taking into account the interplay of magnetic and viscous drag forces, as well as magnetic dipole-dipole and steric interactions. We also consider different configurations of the external magnetic source, in order to optimize bead accumulation and adhesion to the vessel wall in a specific target region, processes that can be driven by magnetic forces.

Keywords: Magnetic biotransport; Magnetic particle; Drug delivery; Drug release; Blood flow; *In silico* model.

1. Introduction

Magnetic nanoparticles (MNPs) and generally magnetic nanomaterials can be advantageously used as contrast agents for magnetic resonance imaging (MRI) [1] or mediators for hyperthermia treatment [2-4], as well as to label, deliver and separate biological samples [5]. This is due to their capability to be manipulated by magnetic fields, independently of biological processes. Large gradient magnetic fields can influence the motion and activities of MNPs in biological media, such as immobilizing them, driving their direction in blood vessels towards a specific area of the body and activate the release of carried drugs in a precise portion of tissue.

Regarding magnetic field source, several methods have been proposed to obtain high magnetic forces with controlled spatial profiles, in order to guide MNPs transport and their release. In most cases the magnetic field is generated by electromagnetic coils or permanent magnets placed outside the body, eventually arranged in arrays to improve MNPs targeting [6-8]. For applications in which magnetic manipulation is required in non-superficial areas, magnetic implant scaffolds have also been proposed [9]. All these studies emphasize the need for a greater understanding of the interplay between magnetic and hydrodynamic forces that act on MNPs circulating in blood vessels, in order to better control their trajectories.

In this scenario, *in silico* models represent an essential tool for predicting the transport of MNPs in blood vessels from their injection to their successive release into target areas [10], providing support to the optimization of both MNPs properties and magnetic source configurations. In Ref. [11] an analytical model was proposed to study the capture of spherical carrier beads with different size, taking into account the effect of the only dominant forces, i.e. the magnetic and the fluidic ones. The magnetic field was assumed to be generated by a magnet of cylindrical shape and infinite extension along the axis orthogonal to the blood vessel. This simple model enables a rapid parametric analysis of magnetic targeting as a function of key parameters like bead size, properties and volume fraction of the embedded magnetic nanoparticles, position, size and magnetization of the magnet, microvessel radius, viscosity and flow rate of blood. Additional effects that have to be included are the interaction forces between beads, like the contact and magnetic dipole-dipole forces, which have an influence on colloidal stability and aggregation phenomena [12,13].

There are also studies that focus on the interaction between particles and vessel wall, e.g. Decuzzi and Ferrari [14] proposed a stochastic approach for predicting the adhesion strength of spheroidal particles in specific contact with a substrate under a linear laminar flow. The probability of adhesion results to be a function of the dislodging hydrodynamic force and of the binding processes, involving the receptors on the vascular endothelial cells and the ligands grafted on the particle surface. Other studies investigate the role of vessel geometry on MNPs transport and distribution, considering as domains of analysis vessel segments reconstructed from medical images [15,16].

Here, we present a numerical model for the simulation of the magnetically driven transport of magnetic nano/microbeads within a 3D microvascular network extracted from a computed tomography (CT) scan. The model combines the Navier-Stokes equations, to simulate blood flow, with classical Newtonian dynamics [17], to calculate the trajectory of each bead. As factors of influence of bead motion, we consider the magnetic force, which is generated by a permanent magnet outside the vessel, the hydrodynamic force, the magnetic dipole-dipole interactions between beads and the steric repulsion effects due to bead surfactant layer, generally added to preserve colloidal stability [18,19].

The model is applied to study the influence of magnet position on the percentage of beads adhering to vessel wall in a specific vessel segment, encapsulated in a target region where we aim at enhancing the release. To analyze the magnet efficacy, we first calculate the surface spatial distribution of the generated magnetic force, focusing on the outward normal component to the vessel wall. We vary the size and position of the magnet to find an optimal configuration that enables us to maximize the magnetic field gradient. Then, we simulate bead transport and release to the target region, as a function of magnet position and bead distribution at the injection site. The overall study is performed for two types of commercial beads, one with size of 300 nm and saturation magnetic moment of about 0.002 pAm^2, the other with size of 1 µm and saturation magnetic moment of about 0.024 pAm^2. All the results are compared to the ones obtained without the external magnetic field source to highlight the role of the magnet in driving bead transport.

2. Physical Model

The transport of magnetic nano/microbeads in a microvascular network is governed by the combined effects of several phenomena, like magnetic forces due to applied magnetic fields, viscous drag forces, gravity, buoyancy, inter-bead effects (e.g. magnetostatic interactions, van der Waals forces, surface coating layers' interactions), perturbations to blood flow, interactions with vessel wall, Brownian motion (negligible for particles larger than a few tens of nanometers) [17]. Here, we consider the main effects only, i.e. the magnetic and drag forces, and the magnetic dipole-dipole and steric interactions, disregarding blood flow perturbations and approximating the adhesion to vessel wall as an inelastic collision [21]. The validity of this assumption was verified a priori by applying the model of contact described in Ref. [14]; in this case, the approach to the vessel wall leads to a succession of collisions, generally characterized by oscillations whose amplitude rapidly reduces.

For the generic i-th bead, velocity $\mathbf{v}_i$ and position $\mathbf{s}_i$ are predicted by means of classical Newtonian dynamics, therefore its trajectory is described by

$$\chi \frac{d\mathbf{v}_i}{dt} = \mathbf{F}_{drag,i} + \mathbf{F}_{mag,i} + \sum_{\substack{j=1 \\ j \neq i}}^{N} \mathbf{F}_{dip,ij} + \sum_{\substack{j=1 \\ j \neq i}}^{N} \mathbf{F}_{ste,ij} \qquad (1)$$

$$\frac{d\mathbf{s}_i}{dt} = \mathbf{v}_i$$

where χ is the bead mass (assumed the same for all the beads), N is the total number of beads, $\mathbf{F}_{drag,i}$ is the viscous drag force, $\mathbf{F}_{mag,i}$ is the magnetic force due to applied magnetic fields, $\mathbf{F}_{dip,ij}$ is the force related to the magnetic dipole-dipole interactions between the i-th and j-th beads and $\mathbf{F}_{ste,ij}$ is the steric repulsive force that occurs when the surfactant layers of the i-th and j-th beads are going to overlap [18, 19]. In the following, the different force contributions are briefly described.

2.1 Drag force

The viscous drag force due to blood flow is expressed by

$$\mathbf{F}_{drag,i} = -6\pi\eta_b R_{hyd}(\mathbf{v}_i - \mathbf{v}_b), \tag{2}$$

where R_{hyd} is the bead hydrodynamic radius, η_b is the blood viscosity and $\mathbf{v}_b$ is the blood velocity. In (2), $\mathbf{v}_i$ and $\mathbf{v}_b$ are calculated at the bead barycenter. The spatial distribution of $\mathbf{v}_b$ in the considered vessel segment is obtained by solving the Navier-Stokes equations for steady-state laminar incompressible flow [10], resulting in

$$\begin{cases} \rho_b\nabla\cdot(\mathbf{v}_b) = 0 \\ \rho_b\mathbf{v}_b\cdot\nabla\mathbf{v}_b = -\nabla p + \eta_b\nabla^2\mathbf{v}_b \end{cases} \tag{3}$$

Boundary condition $\mathbf{v}_b = 0$ is applied on the vessel surface, apart from the vessel cross-sections where the flow enters and gets out. In (3), p is the pressure of blood and ρ_b is its density.

2.2 Magnetic force

The force due to the applied magnetic field $\mathbf{H}_a$ is expressed by

$$\mathbf{F}_{mag,i} = \mu_0(\mathbf{m}_i\cdot\nabla)\mathbf{H}_a, \tag{4}$$

where μ_0 is the permeability of vacuum. The bead is approximated as a point dipole with magnetic moment $\mathbf{m}_i$, described by the Langevin function in the following way

$$\mathbf{m}_i = N_{nano}\mu_{nano}L\left(\frac{\mu_{nano}\mu_0\mathbf{H}_a}{k_BT}\right), \tag{5}$$

where k_B is the Boltzmann constant and T is the absolute temperature. In (5) we assume that the bead is made of N_{nano} non-interacting magnetic nanoparticles, each of them with an amplitude of the magnetic moment defined by μ_{nano} [22]. Parameters N_{nano} and μ_{nano} are used to fit bead magnetization curve [22, 23].

The applied field $\mathbf{H}_a$ is assumed to be generated by an external cylindrical permanent magnet with remanent magnetization M_r, radius a and height b, and it is evaluated in an analytical way [24]. In cylindrical coordinates (ρ, φ, z) with the origin at the magnet barycenter, the field components take the following form

$$H_\rho = M_r[\alpha_+ C(k_+, 1, 1, -1) - \alpha_- C(k_-, 1, 1, -1)]$$

$$H_z = M_r \frac{a}{a+\rho}[\beta_+ C(k_+, \gamma^2, 1, -1) - \beta_- C(k_-, \gamma^2, 1, -1)]$$

with

$$z_\pm = z \pm b/2 \, , \alpha_\pm = \frac{a}{\sqrt{z_\pm^2+(\rho+a)^2}} , \beta_\pm = \frac{z_\pm}{\sqrt{z_\pm^2+(\rho+a)^2}} , \gamma = \frac{a-\rho}{a+\rho} , k_\pm = \sqrt{\frac{z_\pm^2+(\rho-a)^2}{z_\pm^2+(\rho+a)^2}}. \qquad (6)$$

In (6) $C(\cdot, \cdot, \cdot, \cdot)$ is the generalized complete elliptic integral.

2.3 Magnetic dipole-dipole interaction force

Having approximated beads as point dipoles, the magnetic dipole force produced by the j-th bead on the i-th one is determined as

$$\mathbf{F}_{dip,ij} = \frac{3\mu_0}{4\pi r_{ij}^4}[(\mathbf{e}_{ij} \times \mathbf{m}_i) \times \mathbf{m}_j + (\mathbf{e}_{ij} \times \mathbf{m}_j) \times \mathbf{m}_i - 2\mathbf{e}_{ij}(\mathbf{m}_i \cdot \mathbf{m}_j) + 5\mathbf{e}_{ij}(\mathbf{e}_{ij} \times \mathbf{m}_i) \cdot (\mathbf{e}_{ij} \times \mathbf{m}_j)] , \qquad (7)$$

where $\mathbf{r}_{ij} = \mathbf{r}_i - \mathbf{r}_j$ is the vector distance between beads barycenters, with the corresponding unit vector $\mathbf{e}_{ij} = \frac{\mathbf{r}_{ij}}{r_{ij}}$ [19,20]. When the distance between two beads is larger than 12 times the bead radius, we consider the contribution from the dipole-dipole interaction negligible.

2.4 Steric repulsion force

To preserve ferrofluid stability and limit aggregation phenomena, MNPs and magnetic beads are generally coated with a surfactant layer, which is responsible for a steric repulsion force, whose effect becomes important when particles are so close that their coating layers start overlapping [18, 19]. Following Ref. [18] the steric force produced by the j-th bead on the i-th one is expressed by

$$\mathbf{F}_{ste,ij} = \begin{cases} 2\pi k_B T R_s^2 \mathbf{e}_{ij} \frac{n_s}{\delta} ln\left(\frac{2R_{hyd}}{r_{ij}}\right) & \text{for } R_s \leq r_{ij} \leq R_{hyd} \\ 0 & \text{elsewhere} \end{cases} \quad . \tag{8}$$

In (8) n_s is the number of surfactant molecules per unit area on bead surface, R_s is the radius of the solid part of the bead and δ is the surfactant layer thickness. The hydrodynamic radius of the bead is defined as $R_{hyd} = R_s + \delta$.

The steric force is fundamental to avoid the formation of aggregations, which can produce damages to the circulatory system, like blockages in blood vessels.

3. Vessel image acquisition and fluid dynamics simulation

The considered vessel segment is extracted from a computed tomography (CT) scan of a region of the abdomen, acquired from the example data sets of 3D Slicer, an open source software for 3D visualization and processing of medical images [25]. The 3D reconstruction of the vessel segment from the CT scan is performed with the Vascular Modelling Toolkit (VMTK) software, a collection of tools for geometric and surface data analyses for image-based modelling of blood vessels [26]. The selected vessel segment is constituted by an entering branch, from which the blood flow arrives, then dividing into four branches, one of them separating into two branches. The vessel has a cross section with an average diameter of 0.8 mm and extends for a length of about 1.8 cm.

Once the 3D structure is acquired, we discretize the vessel domain with a mesh composed of tetrahedral elements with an average size of 0.9 μm [see Fig. 1(a)]. Then, we obtain the spatial distribution of blood velocity by solving the Navier-Stokes equations (3) with COMSOL Multiphysics® software, which implements a 3D Finite Element Method that approximates velocity components and pressure with quadratic and linear basis functions, respectively.

The fluid dynamics simulation is performed by setting the blood average velocity at 0.75 cm/s, the blood density at 1060 kg/m^3 [27] and the viscosity at 0.005 Ns/m^2. Figure 1(b) shows the calculated blood velocity profile, which is considered in the following as an input for the determination of the viscous drag force during biotransport simulations.
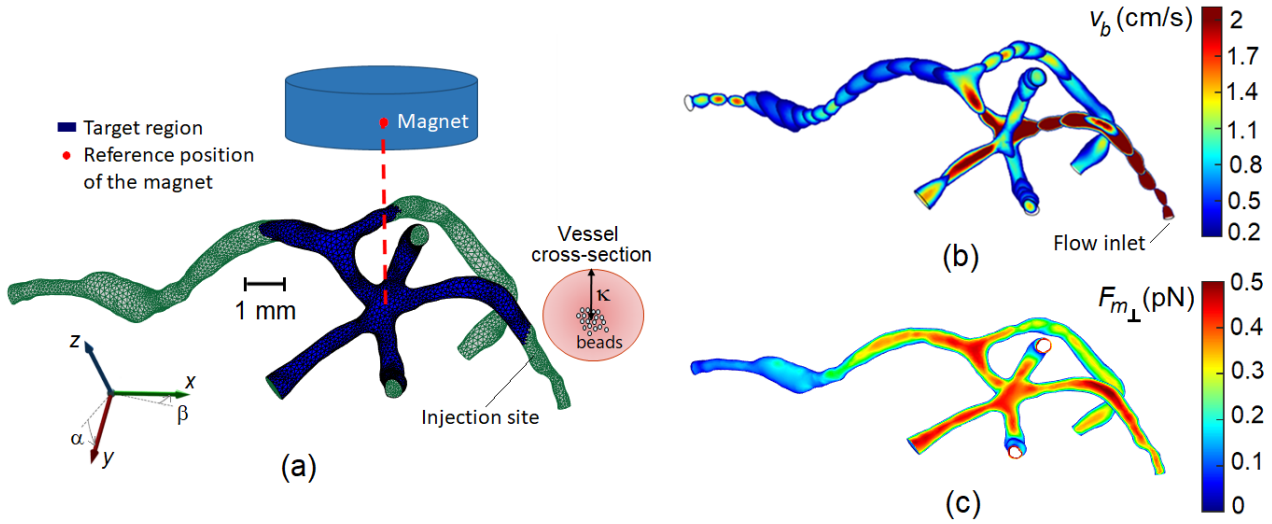
Fig.1. (a) Schematic of the considered blood vessel segment and cylindrical magnet reference position, with indication of the target region for bead adhesion and of the injection site. (b) Blood velocity profile within the vessel. (c) Spatial distribution on the vessel surface of the outward normal component of the magnetic force exerted by a 1.5 cm radius and 2 cm height magnet in reference position, calculated for Dynabeads MyOne bead.

4 Numerical analysis

The modelling study is performed by considering two types of commercial spherical beads for research use only, namely MagSIGNAL (with a 300 nm mean diameter and a saturation magnetic moment of about 0.002 pAm^2) and Dynabeads MyOne (with a 1 μm diameter and a saturation magnetic moment of about 0.025 pAm^2). The first one is composed of 10-15 nm sized ferromagnetic grains dispersed in a silica shell and has a density of 2.5 g/cm^3 [28]; the second one is constituted by a mixture of iron-oxides in a polymeric matrix and has a density of 1.8 g/cm^3 [29]. The magnetic behavior of the two beads is reconstructed by fitting, with Langevin function [5], the experimental magnetization curves provided by the manufactures. For the evaluation of the steric force we assume that the number of surfactant molecules per unit area on bead surface n_s is 10^{15} [27], and the surfactant layer thickness δ is set at 15 nm for MagSIGNAL and 40 nm for Dynabeads MyOne.

The magnetic field source is a cylindrical NdFeB magnet with remanent magnetization fixed to 1000 kA/m, and with a radius a of 1.5 cm and a height b of 2 cm, if not differently specified. In the simulations below, the bottom of the magnet is generally localized at a distance of about 1 cm from the nearest portion of vessel wall. In its reference position [schematized in Fig. 1(a)], the magnet barycenter is located above the middle of the target region, which is defined as the upper part of the wall in the central area of the vessel bifurcation.

4.1 Influence of magnetic source configuration

To investigate magnet efficacy to attract beads in a defined target region, we first calculate the surface spatial distribution of the magnetic force, and in particular of the outward normal component $F_{m_\perp}$ to the vessel wall. The analysis is performed by varying several parameters of the magnet, i.e. size (height and radius), position and inclination with respect to the vessel. The aim is to find the magnetic source configurations that maximize magnetic force, thus increasing the percentage of adhesion to the target region. As an example, Fig. 1(c) reports the surface map of $F_{m_\perp}$ for the magnet reference configuration, calculated for Dynabeads MyOne bead and for a magnet with radius of 1.5 cm and height of 2 cm. The map enables us to find the areas of the vessel wall where the attraction should be stronger (force amplitude in the order of 0.4-0.5 pN for the considered case).

For each considered configuration, we then estimate the average $\bar{F}_{m_\perp}$ of the outward normal component of the magnetic force, determined as the mean value on the surface mesh nodes in the target region. In Fig. 2 we report the maps of $\bar{F}_{m_\perp}$, obtained by varying magnet parameters in the case of Dynabeads MyOne bead. In particular, Fig. 2(a) shows the variation of $\bar{F}_{m_\perp}$ as a function of magnet radius a and height b; here, the x and y coordinates of the magnet barycenter are fixed to the reference position ones, while the z component is modified to guarantee a minimum distance of 1 cm between the magnet bottom and the nearest part of the vessel wall. The highest magnetic forces are reached when the radius is about 1.5 cm and the height is larger than 1.5 cm: the greatest value, in the order of 0.24 pN, is obtained for $b = 3.2$ cm.

In the following analysis, we fix the radius and height of the magnet to the reference values, i.e. $a = 1.5$ cm and $b = 2$ cm, which guarantee an average magnetic force in the target region of about 0.21 pN. The shift of the magnet on the xy-plane leads to the map of $\bar{F}_{m_\perp}$ reported in Fig. 2(b), which shows a quasi-circular symmetry with an increase in the attractive force up to 0.3 pN for displacements along x- and y-axes of about 1 cm. For displacements larger than 2 cm the magnet becomes practically ineffective in the target region: this emphasizes the need for an accurate fine-tuning of its position, achievable with a pre-treatment medical imaging.

The attractive action of the magnet can be increased by modifying its inclination with respect to the vessel wall. As an example, Figs. 2(c) and 2(d) show the change in $\bar{F}_{m_\perp}$ obtained for two different magnet positions when varying angles α and β, which define the orientations with respect to y- and x-axis, respectively, as depicted in the reference frame of Fig. 1(a). In particular, Fig. 2(c) is calculated for Δx=Δy=0, while Fig. 2(d) for Δx = -8 mm and Δy = -6 mm, i.e. the position that leads to the highest magnitude of the average magnetic force, according to Fig. 2(b). In the two maps we can observe ring-shaped areas where $\bar{F}_{m_\perp}$ is larger; for the case with Δx=Δy=0 a maximum force higher than 1 pN

is reached, at the cost of a strong approach of the magnet to the vessel, which limits the possibility of application. For the other case, the highest force value (~0.5 pN) is achieved with $\alpha = 4.6°$ and $\beta = 8°$. The results obtained for Dynabeads MyOne bead, illustrated in Fig. 2, are qualitatively valid also for MagSIGNAL bead, with the significant difference that for the latter the magnetic force amplitude is approximately one order of magnitude lower.
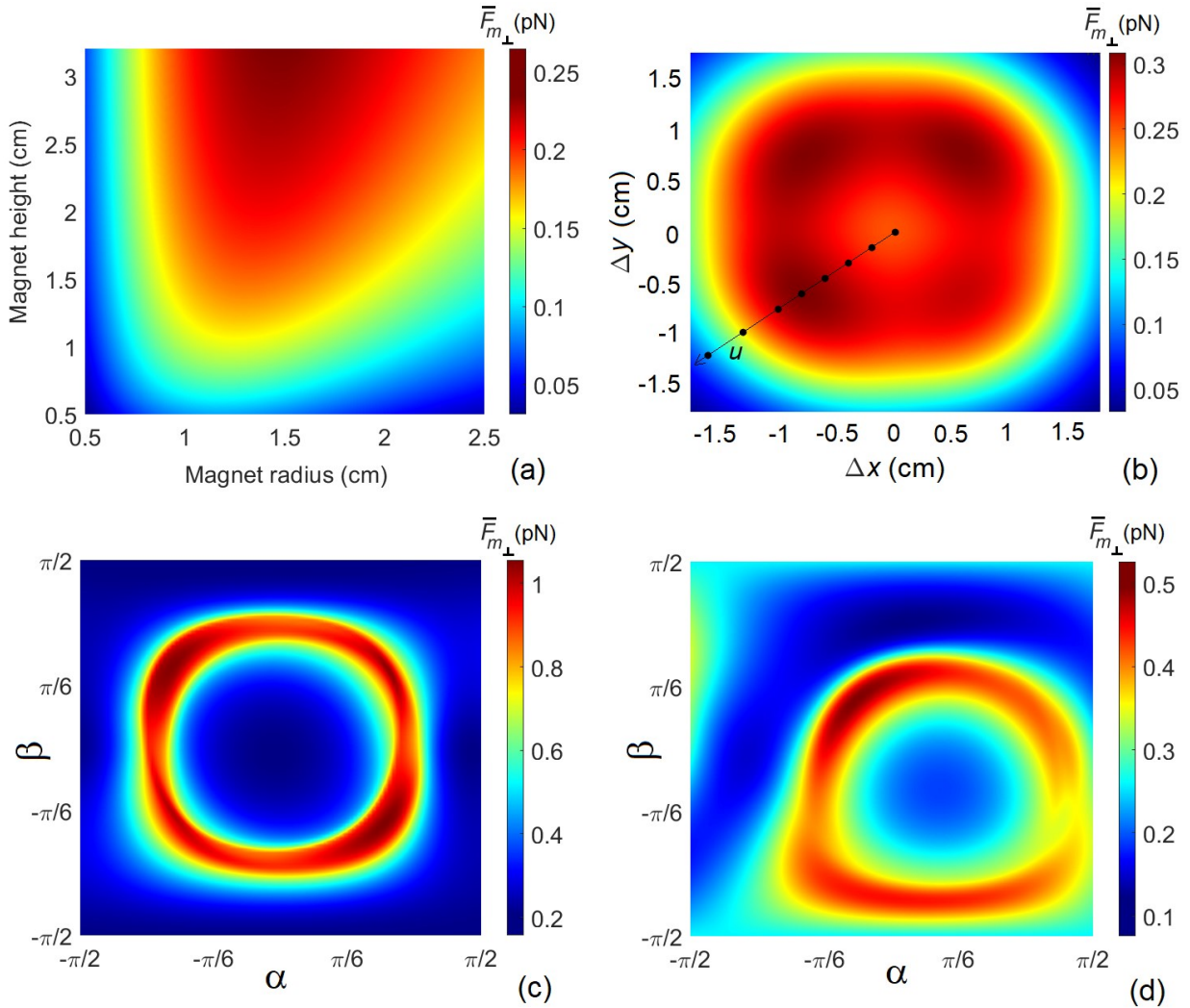

Fig. 2. Maps of the average magnetic force in the target region for Dynabeads MyOne bead. The average is calculated on the outward normal component of the force with respect to the surface of the blood vessel. The study is made by varying: (a) radius and height of the magnet; (b) position of magnet barycenter in the xy-plane (b); magnet inclination with respect to x-axis (angle β) and y-axis (angle α) for the barycenter located (c) at the reference position and (d) shifted ($\Delta x = $ -8 mm, $\Delta y = $ -6 mm). In (b), (c) and (d) the radius and height of the magnet are fixed to 1.5 cm and 2 cm, respectively.
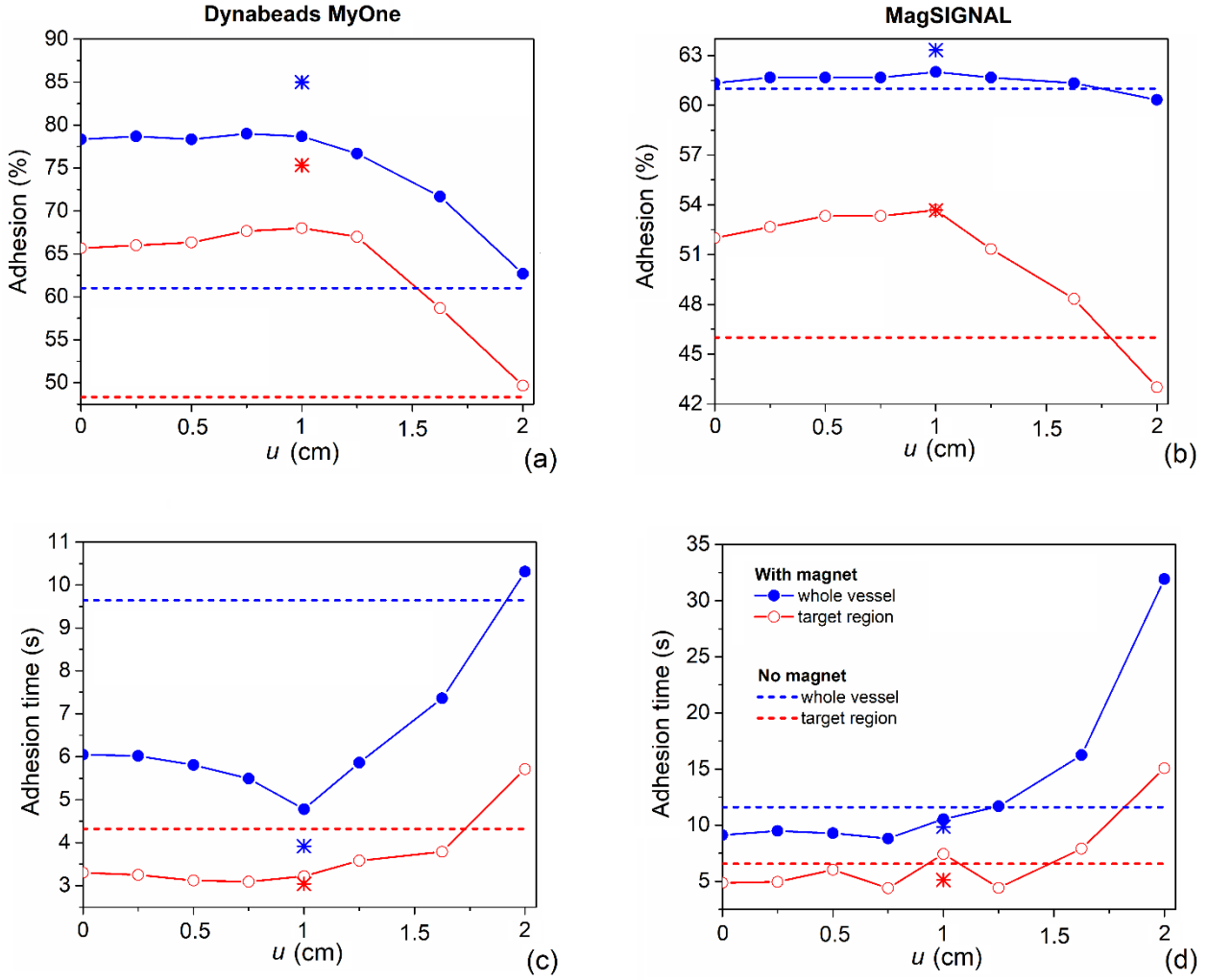
Fig. 3. Results of bead transport simulations for different magnet positions u [Fig. 2(b)], comparing the behavior of Dynabeads MyOne [(a), (c)] and MagSIGNAL [(b), (d)] beads. The plots in (a) and (b) report the percentage of bead adhesion, when an ensemble of 300 identical beads is considered. The plots in (c) and (d) report the average adhesion time per bead. Each graph shows separately the contributions from the whole vessel and the target region only, comparing the results obtained without and with the magnet (with 1.5 cm radius and 2 cm height). The star-shaped markers correspond to the case with the magnet located at $u = 1$ cm and rotated of angles $\alpha = 4.6°$ and $\beta = 8°$ (in blue the result for the entire vessel and in red the one for the target region only).

4.2 Analysis of bead transport and adhesion rate

Here, we investigate magnetic bead transport and rate of adhesion to the target region for the most significant cases previously analyzed, solving systems of equation (1) by means of an implicit variable-order and adaptive step method, based on Numerical Differentiation Formulas (NDFs) [30]. The aim is to study how the position of the magnet and the initial spatial distribution of beads at the vessel inlet influence bead motion and, especially, bead adhesion to the target region. We also compare these results with the ones obtained in the absence of external magnetic fields, to establish the effective role of the magnet on bead adhesion. The simulations are carried out for both bead types,

calculating the trajectories of ensembles of 300 identical beads, from the injection site to release areas or vessel outlets, assuming that the initial velocity of beads is zero. To set the initial positions of the beads, we select an inner volume of the vessel close to the inlet cross-section, where beads are randomly dispersed; this volume represents an ideal injection site indicated in Fig. 1(a).
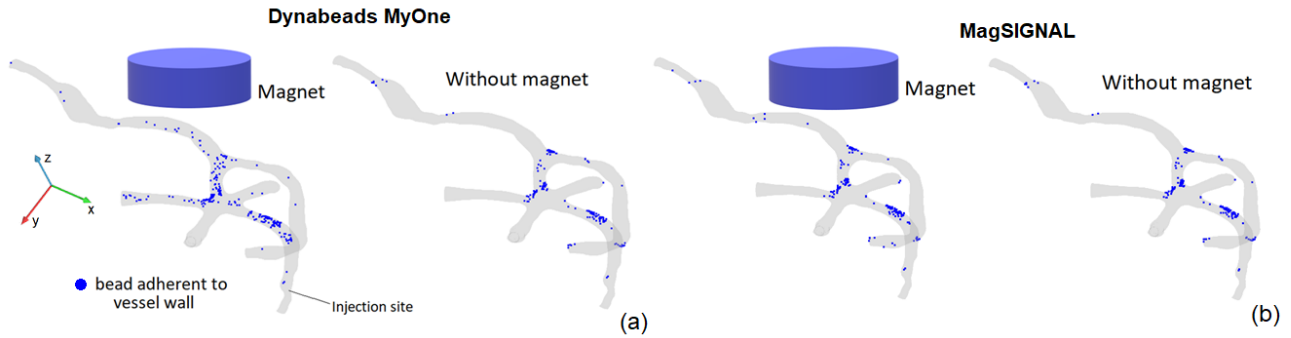

Fig. 4. Schematic representing bead adhesion along the vessel wall, comparing the results obtained for (a) Dynabeads MyOne and (b) MagSIGNAL beads to the relative ones for the case without magnet. The considered magnet has a radius of 1.5 cm, a height of 2 cm and a position in the xy-plane defined by $u = 1$ cm.

Considering the results summarized in Fig. 2(b), we first simulate bead motion for eight different positions of the magnet along the xy-plane, indicated with point markers in the same figure and defined by distance parameter u. For all the configurations, the magnet axis is parallel to z-axis, except for $u = 1$ cm, for which we also consider the case with a non-zero inclination, i.e. $\alpha = 4.6°$ and $\beta = 8°$. In Figs. 3(a) and 3(b) we report the percentages of beads that adhere to the vessel wall versus magnet position u, considering separately the adhesion on the entire vessel wall and in the target region only. For both bead types, the number of beads immobilized on the vessel wall is generally larger when the magnet is present, with a significant enhancement in the target region, which proves the efficacy of the magnet to attract beads in the desired site. The role of the magnet is more evident for Dynabeads MyOne beads, for which a strong increase in the percentage of adhesion can be observed also in the entire vessel, due to the higher value of the magnetic force. The magnet efficacy tends to become negligible for distances from the reference position larger than 1.5 cm, meaning that a fine control of its location is required to drive in an optimized way the bead trajectories. For distances lower than 1.2 cm, no strong variations in the magnet performance are observed by varying u.

When u is set at 1 cm, in the target region Dynabeads MyOne and MagSIGNAL beads have a percentage of adhesion equal to 68% and 54%, respectively, which is a significant increase compared to the 49% and 46% reached in the absence of the magnet. For the case of Dynabeads MyOne, the number of adhesions can be further increased by rotating the magnet; as an example, when $\alpha = 4.6°$ and $\beta = 8°$, a percentage of adhesion of 75% is achieved (see the star-shaped markers in Fig. 3).

As a further study, we evaluate the adhesion time, i.e. the time interval that elapses between the injection of beads in the vessel and the collision to the vessel wall, event in which we consider that beads stop moving. Figures 3(c) and 3(d) show the average time of bead adhesion, as a function of magnet position u; the beads that exit from the vessel through the outlets are not considered in the average calculation. Like the percentage of bead adhesion, also the adhesion time does not exhibit strong variations for distances lower than 1.2 cm, where in most cases the magnet accelerates the approaching to vessel wall, mainly for Dynabeads MyOne. On the contrary, a considerable rise can be observed when u is larger than 1.5 cm, especially for MagSIGNAL. This is again an indication of the loss of magnet efficacy in the considered vessel segment, also proved by the fact that for $u > 2$ cm the average time of adhesion without the magnet is even lower than when it is present. For large values of u, the magnet tries to exert a magnetic force that slows down beads in the blood flow, but at the same time it is too weak to attract them to the vessel wall in the target region. As a result, the number of adhesions in the target region decreases and a higher percentage of beads tends to adhere in peripheral areas, where much more time is needed for targeting. These effects lead to an increase in the average adhesion time and are particularly evident when the difference between the percentage of bead adhesion in the whole vessel and that in the target region is larger.

The role of the magnet for optimal configurations (e.g. $u = 1$ cm) is well illustrated by Fig. 4, which shows the corresponding spatial distribution of beads deposited on the vessel wall, comparing the results obtained for Dynabeads MyOne and MagSIGNAL beads to the ones without the magnet. In the latter, we can notice that the geometrical structure of the vessel has a significant influence on bead distribution, with an enhancement of adhesion in proximity to bifurcations. Under the magnet action, the beads tend to distribute more uniformly, especially in the target region. This effect is less important for MagSIGNAL beads, even if the magnet leads to an increase in the number of adhesions. Finally, we investigate if bead adhesion is affected by the initial spatial distribution of beads at the inlet, considering a fixed magnet configuration ($u = 1$ cm). To this aim, we introduce a parameter κ, which defines the average distance of bead ensemble from the upper part of the vessel wall close to the inlet [see schematic in Fig. 1(a)]. The obtained results are summarized in Fig. 5, which shows the percentage of adhesion as a function of κ (the data reported in the previous figures were calculated with $\kappa \cong 0.17$ mm). Generally, if the beads are initially placed closer to the wall part on the same side of the magnet, a higher number of adhesions can be obtained, putting in evidence the need for a proper selection of the injection site in relation to magnet position and vessel structure. A small reduction in the percentage of adhesion can be observed for very low values of κ, due to the decrease in bead velocity in proximity to the vessel wall. The role of the initial spatial distribution of beads is

more evident for MagSIGNAL beads, due to their weaker reaction to the applied magnetic field and consequent dominance of viscous drag effects.
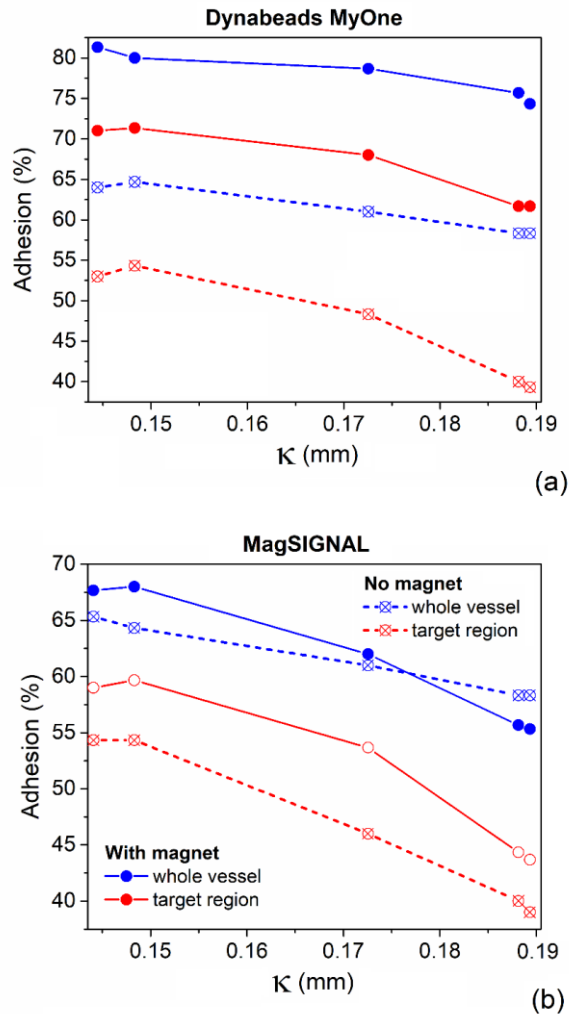

Fig. 5. Results of transport simulations for different spatial distributions of beads at the injection site, obtained by varying parameter κ, i.e. the average distance of beads (at the initial time instant) to the upper part of the vessel wall close to the inlet [Fig. 1(a)]. The figure compares the behavior of (a) Dynabeads MyOne and (b) MagSIGNAL beads, also considering the relative cases without magnet. The plots report the percentage of bead adhesion, when an ensemble of 300 identical beads is considered, showing separately the contributions from the whole vessel and the target region only. The considered magnet has a radius of 1.5 cm, a height of 2 cm and a position in the *xy*-plane defined by $u = 1$ cm.

5. Conclusions

The numerical model presented here allows us to simulate the transport and deposition, under the action of external magnetic fields, of magnetic nano/microbeads that circulate in a 3D segment of a blood vessel reconstructed from medical images. The role of an external cylindrical magnet in driving the motion of beads and their adhesion to a target region has been elucidated, investigating the influence of magnet size and position with respect to the vessel. The magnet has been demonstrated to be more effective for beads with larger size and magnetic moment, due to the dominance of

magnetic force over viscous drag effects. The analysis has also highlighted the need for an accurate fine-tuning of the position of the magnet (to be controlled in the millimeter range) as well as of the bead injection site, in order to enhance the rate of adhesion to a specific target region. In particular, it is evidenced the importance of a priori study of the magnetic force spatial distribution along the vessel wall, in order to find the magnet configuration that leads to larger magnetic field gradients and, consequently, that allows us to increase the number of bead adhesions with reduced time of circulation.

Finally, the developed model has proven to be a useful tool for studying the magnetically driven transport and targeting of magnetic particles in the tissue microvasculature, providing support to the optimization of both particle properties and magnetic source configurations for biomedical applications, like drug delivery.

References

1. J. Estelrich, M. J. Sánchez-Martín, M. A. Busquets, Nanoparticles in magnetic resonance imaging: from simple to dual contrast agents, Int. J. Nanomedicine, 10 (2015), pp. 1727-1741.

2. Z. Hedayatnasab, F. Abnisa, W. M. A. W. Daud, Review on magnetic nanoparticles for magnetic nanofluid hyperthermia application, Materials & Design, 123 (2017), pp. 174-196.

3. M. Bañobre-Lópeza, A. Teijeiro, J. Rivas, Magnetic nanoparticle-based hyperthermia for cancer treatment, Reports of Practical Oncology & Radiotherapy, 18 (6) (2013), pp. 397-400.

4. R. Ferrero, A. Manzin, G. Barrera, F. Celegato, M. Coïsson, P. Tiberto, Infuence of shape, size and magnetostatic interactions on the hyperthermia properties of permalloy nanostructures, Scientific Reports, 9 (2019), 6591.

5. M. Colombo, S. Carregal-Romero, M. F. Casula, L. Gutiérrez, M. P. Morales, I. B. Böhm, J. T. Heverhagen, D. Prosperi, W. J. Parak, Biological applications of magnetic nanoparticles, Chem. Soc. Rev., 41 (2012), pp. 4306-4334.

6. M. D. Tehrani, M. O. Kim, J. Yoon, A Novel Electromagnetic Actuation System for Magnetic Nanoparticle Guidance in Blood Vessels, IEEE Trans. Magn., 50 (2014), 5100412.

7. L. C. Barnsley, D. Carugo, M. Aron, E. Stride, Understanding the dynamics of superparamagnetic particles under the influence of high field gradient arrays, Phys. Med. Biol., 62 (6) (2017), pp. 2333-2360.

8. B. Chertok, A. E. David, V. C. Yang, Brain Tumor Targeting of Magnetic Nanoparticles for Potential Drug Delivery: Effect of Administration Route and Magnetic Field Topography, J Control Release., 155(3) (2011), pp. 393–399.

9. J. Ge, Y. Zhang, Z. Dong, J. Jia, J. Zhu, X. Miao, B. Yan, Initiation of Targeted Nanodrug Delivery in Vivo by a Multifunctional Magnetic Implant, ACS Appl. Mater. Interfaces, 9(24) (2017), pp. 20771-20778.

10. T. Lunnoo, T. Puangmali, Capture Efficiency of Biocompatible Magnetic Nanoparticles in Arterial Flow: A Computer Simulation for Magnetic Drug Targeting, Nanoscale Research Letters, 10 (2015), 426.

11. E. J. Furlani, E. P. Furlani, A model for predicting magnetic targeting of multifunctional particles in the microvasculature, J. Magn. Magn. Mater., 313 (2007), pp. 187-193.

12. D. D. Li, G. H. Yeoh, V. Timchenko, H. Lam, Numerical Modeling of Magnetic Nanoparticle and Carrier Fluid Interactions Under Static and Double-Shear Flows, IEEE Trans. Nanotechnol., 16 (5) (2017), pp. 798-805.

13. A. K. Hoshiar, T.-A. Le, F. U. Amin, M. O. Kim, J. Yoon, Studies of aggregated nanoparticles steering during magnetic-guided drug delivery in the blood vessels, J. Magn. Magn. Mater., 427 (2017), pp. 181–187.

14. P. Decuzzi, M. Ferrari, The adhesive strength of non-spherical particles mediated by specific interactions, Biomaterials, 27 (2006), pp. 5307-5314.

15. A. Patronis, R. A. Richardson, S. Schmieschek, B. J. N. Wylie, R. W. Nash, P. V. Coveney, Modeling Patient-Specific Magnetic Drug Targeting Within the Intracranial Vasculature, Front. Physiol., 9 (2018), 331.

16. A. Boghi, F. Russo, F. Gori, Numerical simulation of magnetic nano drug targeting in a patient-specific coeliac trunk, J. Magn. Magn. Mater., 437 (2017), pp. 86-97.

17. E. P. Furlani, Magnetic Biotransport: Analysis and Applications, Materials, 3 (2010), pp. 2412-2446.

18. A. Satoh, R. W. Chantrell, Application of the dissipative particle dynamics method to magnetic colloidal dispersions, Molecular Physics, 104 (2006), pp. 3287-3302.

19. W. Li, Q. Li, Study about the structure and dynamics of magnetic nanofluids using a mesoscopic simulation approach, Nonlinear Dyn, 91 (2018), pp. 2141-2155.

20. K. W. Yung, P. B. Landecker, D. D. Villani, An analytic solution for the force between two magnetic dipoles, Magn. Electr. Sep., 9 (1998), pp. 39–52.

21. J. W. Haverkort, S. Kenjereš, C. R. Kleijn, Computational Simulations of Magnetic Particle Capture in Arterial Flows, Annals of Biomedical Engineering, 37(12) (2009), pp. 2436–2448.

22. A. Manzin, V. Nabaei, O. Kazakova, Modelling and optimization of submicron Hall sensors for the detection of superparamagnetic beads, Journal of Applied Physics, 111 (2012), 07E513.

23. A. Manzin, V. Nabaei, R. Ferrero, Quantification of magnetic nanobeads with micrometer Hall sensors, IEEE Sensors Journal, 18(24) (2018), pp. 10058–10065.

24. N. Derby, S. Olbert, Cylindrical magnets and ideal solenoids, Am. J. Phys., 78(3) (2010), pp. 229-235.

25. https://www.slicer.org/.

26. http://www.vmtk.org/.

27. S. S. Hossain, T. J. Hughes, P. Decuzzi, Vascular deposition patterns for nanoparticles in an inflamed patient-specific arterial tree, Biomech. Model Mechanobiol., 13(3) (2014), pp. 585–597.

28. http://www.amsbio.com/datasheets/MagSIGNAL-COOH.pdf.

29. http://www.thermofisher.com/order/catalog/product/65011?ICID=sproduct.

30. R. W. Klopfenstein, Numerical differentiation formulas for stiff systems of ordinary differential equations, RCA Rev., 32 (1971), pp. 447–462.